separations

MDPI

Article

Surface Chemical Regulation of Coal Gangue–Rice Husk Biochar for Concurrent Promotion of Hg^{2+} Adsorption and Inhibition of Hg^0 Production

Kaikai Zhang [1,*], Wen Ye [1], Shunquan Shi [2], Jiale Yang [1], Yuyu Zhang [1], Ping Hou [1], Feng Xie [1], Yujie He [1], Jinze Zhao [1] and Shaogang Hu [3,*]

[1] School of Environment and Spatial Informatics, China University of Mining and Technology, Xuzhou 221116, China
[2] China Water Resources Pearl River Planning Surveying and Designing Co., Ltd., Guangzhou 510610, China
[3] Hubei Key Laboratory of Regional Development and Environmental Response, College of Resources and Environmental Science, Hubei University, Wuhan 430062, China
* Correspondence: zhangkk@cumt.edu.cn (K.Z.); hushaogang@hubu.edu.cn (S.H.)

Abstract

Mercury (Hg) is a global pollutant that poses a serious threat to ecosystems and human health. Biochar has shown great potential for mercury removal due to its porous structure and abundant surface functional groups. However, redox-active moieties on biochar can reduce adsorbed Hg^{2+} to volatile Hg^0, leading to secondary mercury dispersion. To suppress this reduction, this study proposes a strategy of co-pyrolyzing coal gangue with rice husk to prepare composite biochars (RHB/CG), leveraging the abundant metal oxides in coal gangue to tailor the surface chemistry of biochar. The materials were characterized by FTIR, Raman, and XRD; static adsorption, mercury speciation analysis, and kinetic experiments were conducted. The results show that coal gangue incorporation significantly enhances the Hg^{2+} adsorption capacity of biochar, with the equilibrium adsorption capacity calculated by the pseudo-second-order kinetic model, increasing from 20.6 mg/g for pristine RHB to 38.7 mg/g for RHB/CG-1:1. More importantly, RHB/CG composites effectively suppress the reduction of Hg^{2+} to Hg^0, and the amount of Hg^0 accumulated in the system is 57.1% lower than that of pristine RHB. Mechanistic studies reveal that coal-gangue-derived basic functional groups (e.g., C–O–C, Si–O–M) inhibit reduction via sequestering Hg^{2+} through coordination and disruption of electron transfer pathways. PHREEQC simulations (pe = 6.0) confirm the decreased tendency of Hg^{2+} reduction to Hg^0 with increasing pH, in good agreement with the experimental results showing reduced Hg^{2+} reduction. The corresponding results provide a green and sustainable solution for mercury-contaminated water and soil remediation.

Keywords: biochar; coal gangue; mercury; PHREEQC

Check for updates

Academic Editors: Jiahui Zhu and Huiquan Gu

Received: 19 May 2026
Revised: 4 June 2026
Accepted: 11 June 2026
Published: 18 June 2026

Copyright: © 2026 by the authors. Licensee MDPI, Basel, Switzerland. This article is an open access article distributed under the terms and conditions of the Creative Commons Attribution (CC BY) license.

1. Introduction

Mercury is a global pollutant that appears as a silvery-white liquid at ambient temperature and pressure and exhibits relatively stable chemical properties [1–3]. Mercury sources can be classified into natural and anthropogenic origins. Forest fires and volcanic eruptions contribute significantly to the natural release of mercury [4–7]. Anthropogenic sources are dominated by industrial activities, for instance, mining, coal-fired power generation, cement production, and the chlor-alkali industry [8–10]. Among these, historic Ag mining

and production was the largest single source of anthropogenic mercury (Hg) to the environment, contributing several times more Hg to the atmosphere (146 kt, 31% of total emissions) than combined industrial and artisanal gold (Au) production (55.4 kt) or coal combustion (26.4 kt) [2,11]. Mercury production, much of which was destined for use in small-scale Ag and Au mining, contributed the second highest amount (91.7 kt) [12–14]. Such historical releases have led to ongoing contamination. For instance, in the Cauca Department of Colombia, a region known for its intensive artisanal and small-scale gold mining activities, mercury concentrations in surface water have reached as high as 0.05 mg/L [15]. In the Arequipa region of Peru, mercury and other metals have been detected in tailings and wastewater from gold cyanidation facilities [16]. Beyond mining, the chlor-alkali industry, which once widely used mercury cathode electrolysis to produce chlorine and caustic soda, generated wastewater with total mercury levels ranging from 1.6 to 7.6 mg/L [17]. Once released into the environment, Hg^{2+} and Hg^0 become available to microorganisms. These microorganisms can methylate them into methylmercury [18–20]. Methylmercury is highly neurotoxic and readily undergoes biomagnification along food chains, posing significant risks to both humans and wildlife [21,22]. Therefore, curbing the generation and improper discharge of mercury pollution at the source and interrupting the migration pathways of mercury are key strategies for tackling the global mercury issue.

To control mercury release at the source and block its migration, multiple materials have been developed to reduce mercury risks through adsorption, such as biochar [23], carbon nanotubes [24], kapok fiber [25], sulfur-enriched adsorbents [26], and palm oil fuel ash [27]. However, these materials differ substantially in performance, each presenting distinct advantages and limitations. Carbon nanotubes possess a high specific surface area, a unique pore structure, and good stability, yet their practical use is limited by high preparation costs, poor dispersibility in water, and difficult recovery [28]. Natural biomass materials like kapok fiber are low-cost and widely available, but their pristine adsorption capacity for Hg^{2+} is rather low (39.9 mg/g), and reaching a much higher capacity (235.7 mg/g) requires additional dopamine surface modification, which adds complexity [25]. Palm oil fuel ash, an agricultural waste, is inexpensive; nevertheless, its mercury adsorption performance is constrained by unfavorable surface properties and pore structure, resulting in a relatively low adsorption capacity [27].

Biochar is a carbonaceous material produced by pyrolyzing biomass under oxygen-limited atmospheres [29]. Owing to its large specific surface area, developed porous structures, abundant oxygen-containing functional groups, low cost and good recyclability, biochar has been widely used in soil remediation [30,31], wastewater treatment [32,33], and soil amendment [34,35]. In mercury removal, the surface functional groups of biochar can enhance its adsorption capacity. For instance, thiol groups exhibit a strong affinity for mercury and can improve biochar's cation exchange capacity, thereby facilitating mercury immobilization [26,36]. However, the adsorbed Hg^{2+} can be reduced to Hg^0 by redox-active moieties in biochar, such as dissolved black carbon (DBC, i.e., the biochar fraction passing through a 0.1–0.7 μm filter), as well as aromatic moieties and quinone–hydroquinone functional groups on particulate biochar [37,38]. This reduction process drives the production of volatile Hg^0, thereby causing the re-release and diffusion of mercury. Therefore, more effective modification strategies need to be developed to reduce the risk of mercury reduction and subsequent re-release from biochar.

Despite extensive research on mercury adsorption, the vast majority of existing studies have focused exclusively on maximizing adsorption capacity, while the reduction pathway of adsorbed Hg(II) has been largely overlooked. Several studies have documented that commonly used adsorbents inadvertently promote this unintended reduction. For instance, 5 mg C/L dissolved black carbon from biochar facilitated Hg(II) photoreduction to Hg^0 un-

der simulated sunlight, with a reduction ratio of 73 ± 4% within 5.3 h [37]. C=C/C-C/C-H moieties on particulate biochar and dissolved black carbon drove Hg(II) reduction with 0.06–2.16 L $mg^{-1}h^{-1}$ of the reaction rate constant [38]. Zero-valent iron induced inevitable Hg^0 escape, originating from a 34–72% reduction in adsorbed Hg(II) reduction [39]. To date, few strategies have been reported that simultaneously achieve efficient Hg(II) adsorption while effectively inhibiting its post-adsorption reduction. Accordingly, a critical but previously unrecognized limitation of existing remediation materials is that they passively permit, or even actively promote, the unintended reduction of adsorbed Hg(II) to volatile Hg^0, creating a secondary pollution pathway that has not been systematically addressed.

To address the risk of mercury reduction and re-release during mercury adsorption by biochar, this study proposes a strategy of preparing modified biochar through the co-pyrolysis of coal gangue and rice husk, aiming to suppress Hg^{2+} reduction at the source. Unlike conventional methods such as wet chemical impregnation or post-synthesis loading of metal oxides, which rely on physical adsorption or weak surface interactions, co-pyrolysis enables in situ integration of metal elements from coal gangue with the carbonaceous framework of biomass [40] while simultaneously promoting the formation of a well-developed mesoporous structure [41]. Coal gangue is selected as the modifier because its abundant metal oxides can play dual regulatory roles during pyrolysis [42,43]. On one hand, these metal oxides can act as catalysts to promote the thermochemical conversion of lignocellulose in rice husk, thereby optimizing the pore structure of the biochar and generating a developed mesoporous system. This provides efficient mass transfer channels for Hg^{2+} and increases surface adsorption sites. On the other hand, the introduced metal active sites, such as Si-O, Al-O, and Fe-O, exhibit strong coordination affinity toward Hg^{2+}. They are expected not only to enhance the adsorption capacity but also to effectively inhibit the reduction of Hg^{2+} driven by redox-active moieties of biochar. This study investigates the influence of coal gangue on the physicochemical properties of modified biochar. Both static and kinetic mercury adsorption experiments, as well as mercury speciation analysis, are conducted. These experiments elucidate the mechanisms by which coal gangue modification regulates mercury adsorption and reduction. Corresponding results can provide a novel insight into the development of biochar-based materials for mercury pollution remediation.

2. Materials and Methods

2.1. Materials

Rice husk was obtained from Nongzi Horticulture (Harbin, China). Coal gangue was supplied by Chuanyi Mining Co., Ltd. (Taiyuan, China). Mercury(II) chloride (analytical grade), nitric acid (analytical grade), hydrochloric acid (analytical grade), potassium permanganate (analytical grade), and sodium hydroxide (analytical grade) were purchased from Beijing Tongguang Fine Chemical Company (Beijing, China), Shanghai Macklin Biochemical Technology Co., Ltd. (Shanghai, China), and Beijing Tongguang Fine Chemical Company as specified. A vacuum tube furnace (model ZSK1200, Xinnite Electric Furnace Co., Ltd., Beijing, China) was used for biochar preparation. A pH meter (model FE28-Standard, Mettler-Toledo, Greifensee, Switzerland) was employed for pH measurement. A cold vapor atomic absorption mercury analyzer (model F732-V, Shanghai Huaguang Instrument Co., Ltd., Beijing, China) was used for mercury concentration determination. X-ray diffraction (XRD) patterns were recorded on a D/max-2550 diffractometer (Rigaku Corporation, Tokyo, Japan). Fourier transform infrared (FTIR) spectra were obtained using a Nicolet 6700 spectrometer (Thermo Nicolet Corporation, Madison, WI, USA). Raman spectra were collected on a LabRAM HR Evolution Raman spectrometer (Horiba, Paris, France).

2.2. Biochar Preparation and Characterization

The mineral composition and proportion of coal gangue (CG) regulate the inorganic framework, catalytic behavior, and elemental doping of the composite biochar, while the biomass components, high-silicon nature, and amount of rice husk (RH) provide the organic carbon precursor and a porous silicon template. The mass ratio of CG to RH directly determines the organic/inorganic phase ratio and the intensity of their interactions. A pyrolysis temperature of 600 °C, holding time of 2 h, and N_2 flow rate of 5 mL/min were used for biochar preparation. Through complex interactions, composite biochars with unique structure and properties were obtained. Optimized preparation aims to balance and maximize these interactions by adjusting the CG/RH ratio.

The biochars were prepared via oxygen-limited high-temperature pyrolysis. Rice husk was first dried, crushed, and then sieved through a 100-mesh sieve to obtain a uniform particle size. The sieved rice husk was then mixed with coal gangue at four different rice-husk-to-coal-gangue (RH:CG) mass ratios: pure RH (no CG), 10:1, 5:1, and 1:1, corresponding to 50 g RH + 5 g CG, 50 g RH + 10 g CG, and 30 g RH + 30 g CG, respectively. Each mixture was placed in a tube furnace and heated at 600 °C for 2 h under a N_2 flow of 5 mL/min, a temperature previously shown to optimize biochar adsorption performance [44]. After pyrolysis, the resulting biochars were allowed to cool to room temperature under a N_2 atmosphere and then were sieved through a 100-mesh sieve for subsequent adsorption experiments and characterization. The prepared samples are denoted as RHB (pure rice husk biochar) and RHB/CG-10:1, RHB/CG-5:1, and RHB/CG-1:1 according to the CG:RH mass ratio.

The crystal structure and phase composition of the four adsorbents were determined by X-ray diffraction (XRD) using a D/max-2550 diffractometer (Rigaku, Tokyo, Japan). Spectra were recorded over a scanning range of 5–85° at a scanning speed of 5°/min. Fourier transform infrared (FTIR) spectra were obtained on a Nicolet 6700 spectrometer (Thermo Nicolet Corporation, Madison, WI, USA) in transmission mode over a wavenumber range of 4000–400 cm^{-1} with a resolution of 4 cm^{-1} to identify surface functional groups. Raman spectra were collected on a LabRAM HR Evolution Raman spectrometer (Horiba, Paris, France) using a 785 nm laser excitation wavelength and 50 mW laser power over a wavenumber range of 50–2000 cm^{-1} to evaluate the molecular structure and carbon defect degree of the biochars.

2.3. Hg^{2+} Adsorption Capacity

A $HgCl_2$ stock solution (100 mg Hg(II)/L) was prepared by dissolving 1.3536 g of $HgCl_2$ solid in acidified deionized water containing 5% HNO_3 and 5% HCl (unless otherwise stated, this acidified water was used for all subsequent dilutions). The stock solution was properly labeled and stored for later adsorption experiments. The working standard solution (1 mg/L Hg(II)) was obtained by diluting the stock solution 100-fold with the same acidified water.

Before the systematic adsorption tests, a preliminary adsorption experiment was conducted to evaluate the performance of the prepared materials. First, the Hg(II) solution was diluted to 1 mg/L and its pH was adjusted to approximately 4.0 ± 0.2. Then, 2 mg of each prepared biochar (or adsorbent) sample was weighed into a 50 mL stoppered conical flask, The flasks were placed in a thermostatic shaker and shaken for 2 h under default conditions (25 °C, 180 r/min). After shaking, an aliquot of the suspension was withdrawn using a syringe, filtered through a 0.22 μm membrane filter, and appropriately diluted, and the residual Hg^{2+} concentration was determined by cold vapor atomic absorption spectrometry. The equilibrium adsorption capacity (Q_e, mg/g) was calculated using Equation (1):

$$Q_e = \frac{(C_0 - C_e)V_L}{W} \quad (1)$$

where C_0 (mg/L) and C_e (mg/L) are the initial and equilibrium Hg(II) concentrations, respectively. V_L is the volume of the $HgCl_2$ solution used. W is the mass of the adsorbent. All dilutions of mercury solutions were performed gravimetrically to minimize experimental errors.

2.4. Hg^{2+} Adsorption Kinetics

A $HgCl_2$ solution with an initial concentration of 1 mg/L was prepared by diluting the mercury stock solution, and its pH was adjusted to 4.0 ± 0.2. Then, 2 mg of each adsorbent was added to a beaker containing 100 mL of the 1 mg/L Hg^{2+} solution. The mixture was stirred at room temperature (25 °C) at 180 r/min for 120 min. At specific time intervals (0, 15, 30, 45, 60, 90, and 120 min), an aliquot of the suspension was withdrawn using a syringe, filtered through a 0.22 μm membrane filter, and appropriately diluted, and the residual Hg^{2+} concentration was determined by cold vapor atomic absorption spectrometry. The amount of Hg^{2+} adsorbed per unit mass of adsorbent at a specific time, $Q_e(t)$ (mg/g), was calculated using Equation (1). The kinetic data were fitted by the pseudo-first-order and pseudo-second-order kinetic models. The non-linear expressions of the two models are given as follows:

Pseudo-first-order model:

$$\frac{dq}{dt} = k_1(q_e - q_t) \quad (2)$$

Pseudo-second-order model:

$$\frac{dq}{dt} = k_2(q_e - q_t)^2 \quad (3)$$

where q_e (mg/g) and q_t (mg/g) are the adsorption capacities of the adsorbent at equilibrium and at time t. k_1 (min^{-1}) and k_2 ($g \cdot mg^{-1} \cdot min^{-1}$) are the rate constants of the pseudo-first-order and pseudo-second-order models, respectively.

2.5. pH Effect on Hg^{2+} Adsorption

The influence of solution pH on Hg^{2+} adsorption was investigated for the four biochar materials, including RHB, RHB/CG-10:1, RHB/CG-5:1, and RHB/CG-1:1. A series of 100 mL aliquots of $HgCl_2$ solution (initial Hg^{2+} concentration 1 mg/L) were placed in stoppered conical flasks, and the pH of each aliquot was adjusted to a value in the range of 2.0–12.0 using NaOH or HCl solution. Then, 2 mg of each adsorbent was added to the flasks. The mixtures were stirred at room temperature (25 °C) at 180 r/min for 2 h. After stirring, approximately 1 mL of the suspension was withdrawn with a syringe, filtered through a 0.22 μm membrane filter, and appropriately diluted, and the residual Hg^{2+} concentration was determined by cold vapor atomic absorption spectrometry. The adsorption capacity of each material at each pH was calculated using Equation (1), and the optimal pH for Hg^{2+} removal was identified by comparing the capacities across the pH range.

2.6. Hg^{2+} Reduction Assessment

After the above adsorption experiments, the reducing ability of RHB and RHB/CG-1:1 toward Hg^{2+} was evaluated. The experimental setup is illustrated in a previous study [38]. An amount of 100 mg of adsorbent was added to a three-necked flask containing 100 mL of 1 mg/L Hg^{2+} solution. The flask was purged with N_2 and sealed, then stirred at 180 r/min in a constant-temperature water bath (25 °C) for 120 min. Downstream, an oxidation bottle containing $KMnO_4$ solution was connected to trap the reduced Hg^0, followed by a diluted

HNO_3 solution for tail gas collection. At selected time intervals (0, 15, 30, 45, 60, 90, and 120 min), approximately 1 mL of solution was withdrawn from both the three-necked flask and the oxidation bottle using a syringe, and filtered through a 0.22 μm membrane filter. After appropriate dilution, the Hg^{2+} concentration in the three-necked flask and the Hg^0 concentration (as oxidized Hg^{2+} in the oxidation bottle) were determined by cold vapor atomic absorption spectrometry, allowing the simultaneous monitoring of Hg^{2+} depletion and Hg^0 generation over time.

2.7. PHREEQC Geochemical Modeling

All geochemical simulations were performed using PHREEQC (version 3.7.3, developed by the U.S. Geological Survey). Because the default databases (e.g., phreeqc.dat, wateq4f.dat) do not contain thermodynamic data for mercury, the minteq.v4.dat database was selected. This database, originally derived from the USEPA's MINTEQA2 code, includes comprehensive stability constants for Hg(II) and its chloride complexes.

Aqueous solutions were prepared with 1 mg/L Hg^{2+} and 0.35 mg/L Cl^-. The effect of pH on mercury speciation was examined over a pH range of 2.0, 3.0, 4.0, 5.0, 6.0, 7.0, 8.0, 9.0, 10.0, 11.0, and 12.0. All simulations were conducted at 25 °C. The redox potential was fixed at pe = 6.0. The PHREEQC input file was constructed using keyword data blocks. The main blocks included DATABASE, which specifies the path to the minteq.v4.dat file; SOLUTION, which defines individual solutions for each pH value using the parameters of temperature (25 °C), pH (x.0), pe (6.0), concentrations in mg/L (Hg: 1.0, Cl: 0.35), and water mass (1 kg); and SELECTED_OUTPUT, which requests the output of pH, total concentrations of Hg and Cl, and molalities of all relevant Hg species. A total of 11 SOLUTION blocks (pH 2.0 to 12.0) were included, and each solution was equilibrated separately. After each simulation, the output file provided molal concentrations (mol/kgw) of individual mercury species. The mole percentage of each species was calculated by dividing its molality by the total mercury molality.

3. Results and Discussion

3.1. Coal Gangue Altering Carbon Composition

The incorporation of coal gangue predominantly regulated the surface chemical functionality of the biochar, particularly the distribution of oxygen-containing moieties and mineral-associated structural units, whereas its effect on the carbonaceous backbone was comparatively limited. FTIR spectra (Figure 1a) provide direct evidence for the evolution of surface functional groups after coal gangue incorporation. All biochar samples exhibited a broad band centered at approximately 3430 cm^{-1}, which is characteristic of the stretching vibration of hydroxyl groups (–OH), suggesting the presence of surface hydroxyl functionalities and physically adsorbed water [45]. The adsorption band near 1435 cm^{-1} can be attributed to the symmetric stretching of carboxylate groups ($–COO^-$), reflecting the possible presence of carboxylate-related structures on the surface [46]. Notably, the absorption bands near 1017 cm^{-1} and 879 cm^{-1} can be attributed to C–O related vibrations, indicating the presence of oxygenated organic structural units such as phenolic hydroxyl, alcoholic hydroxyl, and ether groups [47]. In addition, the absorption band in the low-wavenumber region, particularly near 695 cm^{-1} and 470 cm^{-1}, is associated with Si–O–Si/Si–O–Al and Al/Fe–O vibrations [48], indicating the incorporation of aluminosilicate mineral structures derived from coal gangue into the composite samples.

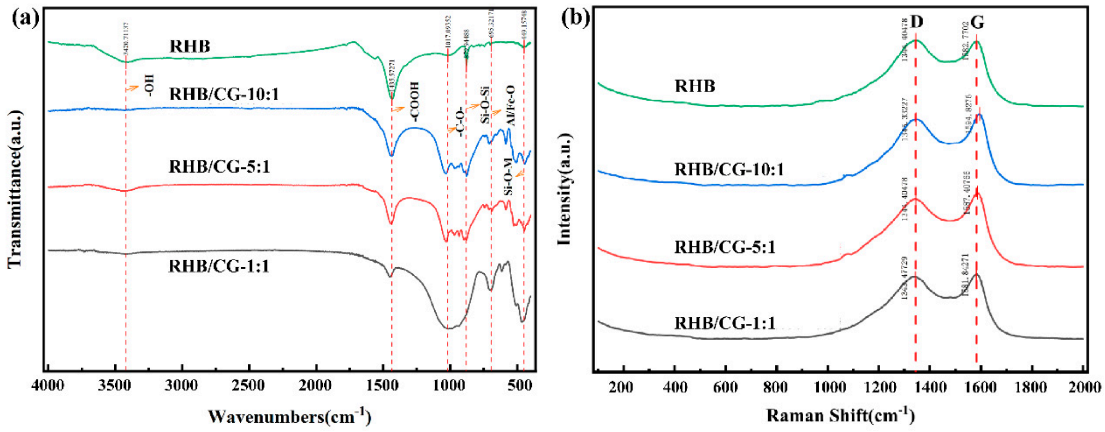


Figure 1. (**a**) FTIR spectra and (**b**) Raman spectra of rice husk biochar (RHB) and rice husk biochar/coal gangue composite adsorbents with different mass ratios (RHB/CG-10:1, RHB/CG-5:1, and RHB/CG-1:1). Dashed lines indicate the peak positions observed in the spectra.

Compared with pristine RHB, the composite biochars exhibited pronounced changes in both the intensity and profile of the above characteristic bands, indicating that the addition of coal gangue significantly altered the surface functional group composition and chemical environment. Specifically, with increasing coal gangue content, the absorption feature near 470 cm^{-1} associated with Al/Si–O gradually intensified, suggesting that aluminosilicate mineral components from coal gangue were effectively retained and loaded onto the biochar surface. Meanwhile, coal gangue significantly influenced the evolution of surface-oxygen-containing functionalities during co-pyrolysis. For instance, the increase trends observed at 1017 cm^{-1} and 879 cm^{-1} and the decrease at 1435 cm^{-1} demonstrated that the incorporation of coal gangue also modified the content and distribution of C–O- and $–COO^{-}$-containing functional groups. These variations suggest that coal gangue not only introduced inorganic mineral phases into the biochar matrix but also participated in the transformation and redistribution of oxygenated organic moieties through interactions between gangue-derived mineral components and biomass pyrolysis intermediates.

In contrast, the Raman spectra suggest that coal gangue had a comparatively minor effect on the carbon structure of the biochar. All samples exhibited the typical D band and G band at approximately 1340 cm^{-1} and 1590 cm^{-1} (Figure 1b), respectively, corresponding to defect-rich disordered carbon and sp^2-hybridized graphitic carbon [49,50]. This indicates that the carbon phase of all samples remained dominated by aromatic structures with a substantial degree of disorder, which is characteristic of pyrolytic biochar. Notably, the positions and overall spectral profiles of the D and G bands showed no obvious changes after coal gangue incorporation, indicating that the fundamental aromatic carbon skeleton remained largely preserved during composite formation. This interpretation is further supported by the Raman fitting results. As shown in Table 1, upon the addition of coal gangue, the gradual increase in I_D/I_G from 3.03 to 3.42 indicates that the proportion of defect sites or disordered carbon domains increased slightly with increasing gangue content, suggesting that coal gangue exerted a certain perturbation on the local ordering and rearrangement of carbon micro-crystallites during pyrolysis. However, the magnitude of this variation remained limited, and no significant band shift or drastic spectral broadening was observed. This demonstrates that coal gangue did not fundamentally alter the carbonization pathway of the biochar, nor did it markedly promote graphitization or induce severe disruption of the carbon framework. Rather, its influence on the carbon phase was mainly manifested as a slight increase in structural defects rather than an essential reconstruction of the carbon skeleton.

Table 1. Raman-derived I_D/I_G ratios of different biochars.

Biochar	A_D	A_G	I_D/I_G
RHB	53,754.95	17,684.47	3.03
RHB/CG-10:1	53,293.24	16,488.60	3.23
RHB/CG-5:1	53,357.03	15,608.48	3.41
RHB/CG-1:1	60,030.44	17,517.67	3.42

3.2. Formation of Metal Oxides on Biochar

The incorporation of coal gangue altered the mineral phase composition of the biochar (Figure 2) and thereby promoted the in situ formation of metal oxide-related phases during co-pyrolysis. As shown in Figure 2a–d, all biochar samples showed broad diffraction humps centered at around 22° and 25°, indicating that the biochars were predominantly composed of amorphous carbon and amorphous SiO_2 [48,49]. In pristine RHB, characteristic peaks assigned to $Na_2CO_3 \cdot H_2O$ were observed at around 36° and 45° (PDF#37-0451), suggesting that the mineral fraction of the original biochar mainly consisted of silica and sodium-containing salts. After the addition of coal gangue, however, new crystalline phases emerged, revealing significant mineral transformation within the composite system. Specifically, in RHB/CG-10:1, the appearance of $NaSiO_3$ at around 36° (PDF#00-001-1047) and $CaFeO_3$ at approximately 33° and 39° (PDF#01-078-6572) indicates that coal gangue promoted the interaction of silica with alkali and metal species, resulting in the conversion of part of the original SiO_2 into new silicate and metal oxide-related phases (Figure 3a). With further increasing gangue content, the characteristic peaks of $Ca_2Fe_{22}O_{33}$ detected at around 28° and 33° in RHB/CG-5:1 suggest that these metal-containing phases underwent further reaction to form more complex oxide structures [51]. In RHB/CG-1:1, the emergence of $KNa_3(AlSiO_3)$ at approximately 21° and 30° (PDF#84-149) further confirms that a higher gangue ratio intensified the reconstruction of silica-related structures and facilitated the generation of more complex metal-containing mineral phases. Overall, these results demonstrate that coal gangue did not simply act as an inert additive but actively participated in the mineral evolution of the biochar by transforming Si-containing structures and introducing metal ions that favored the formation of Si–O–M linkages and metal oxide-related compounds. Such structural evolution is expected to increase the number of adsorption active sites, enhance surface heterogeneity, and ultimately contribute to the improved adsorption performance of the composite biochars.

3.3. Coal Gangue Promoting Hg^{2-} Adsorption

Hg^{2+} adsorption on RHB and RHB/CG composite biochars exhibited a typical fast-to-slow kinetic behavior before reaching equilibrium. As shown in Figures 3b and 4a–d, the adsorption capacity of all samples increased rapidly during the initial 20–30 min, and then the growth rate gradually slowed until adsorption equilibrium was nearly reached within 60–120 min. This trend suggests that a large number of active sites were available at the beginning of the adsorption process, enabling rapid Hg^{2+} uptake, while the subsequent decrease in adsorption rate was mainly caused by the gradual occupation of these sites.

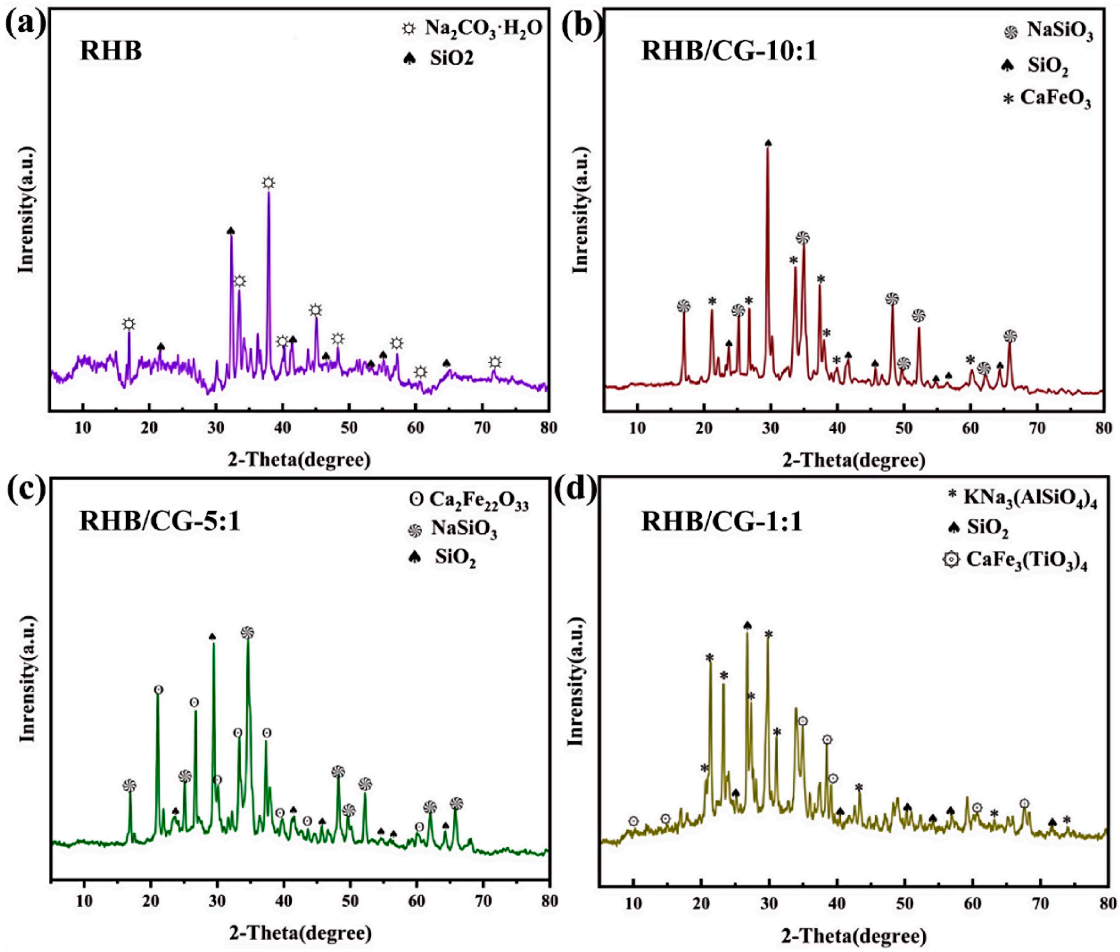


Figure 2. XRD patterns of RHB (**a**), RHB/CG-10:1 (**b**), RHB/CG-5:1 (**c**) and RHB/CG-1:1 (**d**).

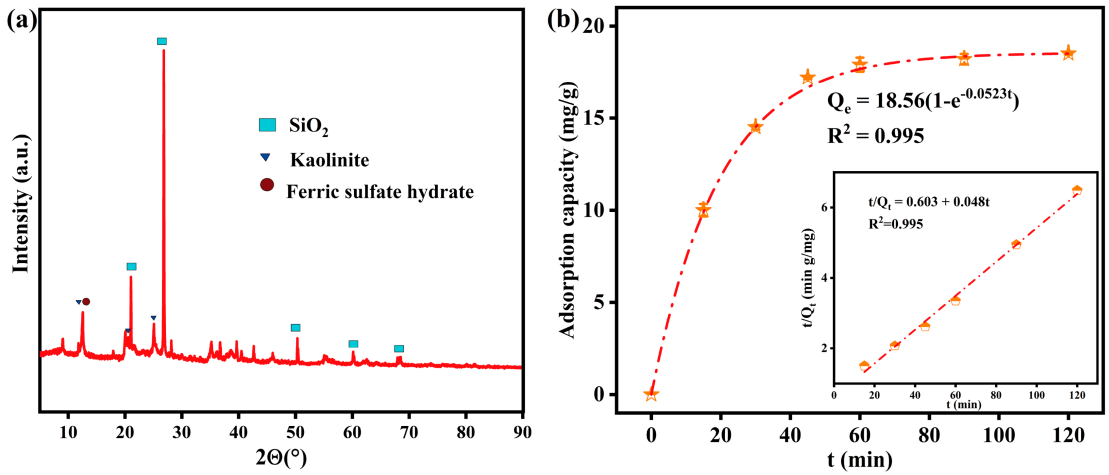


Figure 3. (**a**) XRD pattern of coal gangue in the present study. (**b**) Adsorption kinetics of Hg^{2+} on coal gangue. In panel (**b**), the symbols represent experimental data, and the red dashed-dotted line represents the fit for the pseudo-second-order model. The inset shows the linear plot of the pseudo-first-order model. Error bars represent the standard deviation of three replicates.

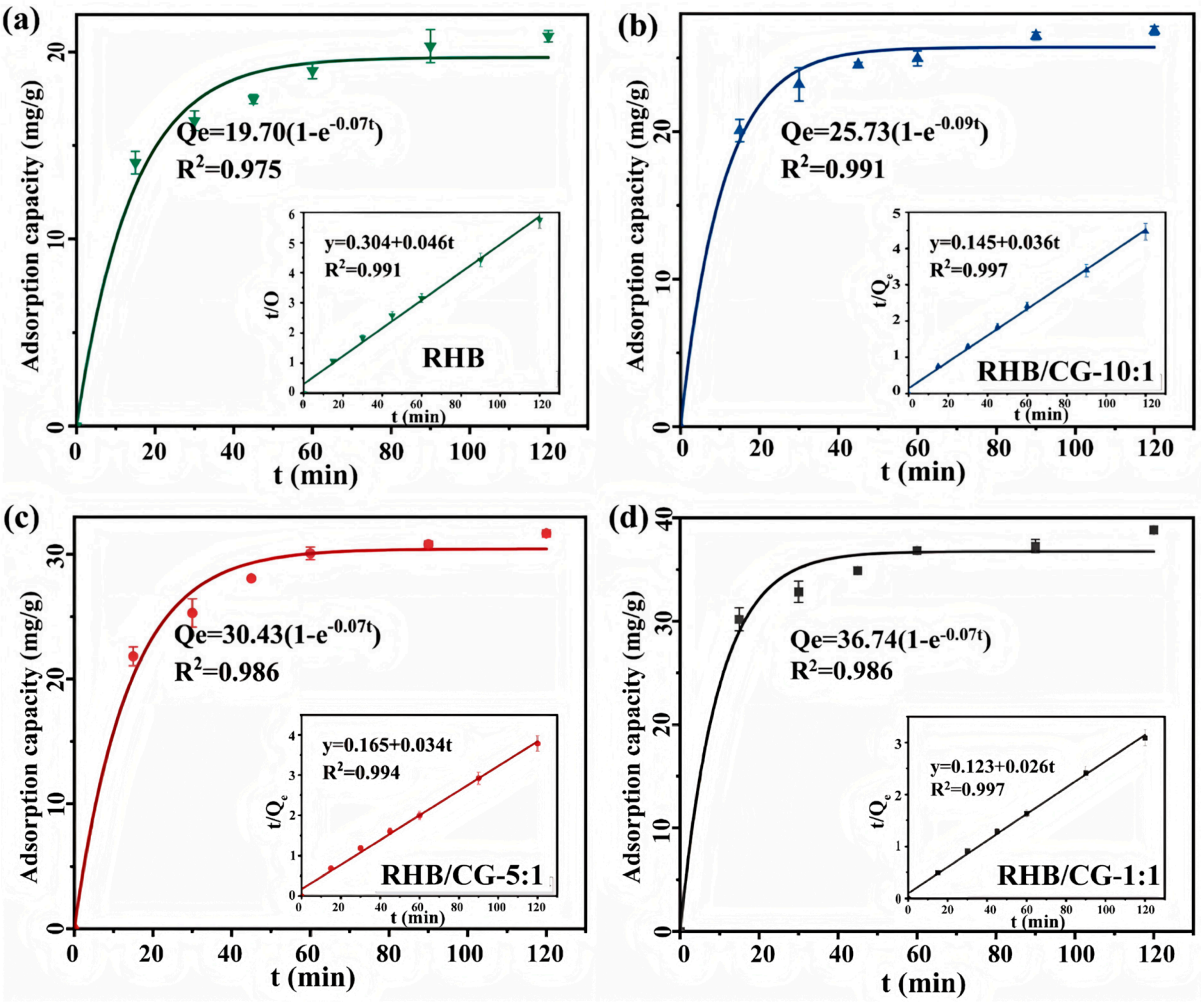


Figure 4. Adsorption kinetics of Hg^{2+} on (**a**) RHB, (**b**) RHB/CG-10:1, (**c**) RHB/CG-5:1, and (**d**) RHB/CG-1:1.

The pseudo-second-order model provided a better description of the Hg^{2+} adsorption kinetics than the pseudo-first-order model, which indicates that chemisorption is the overall rate-controlling step [52]. According to Table 2, although both models showed relatively high fitting coefficients, the pseudo-second-order model consistently exhibited higher R^2 values (0.991–0.997) than the pseudo-first-order model (0.975–0.991) for all adsorbents. Meanwhile, the equilibrium adsorption capacities at 1 mg/g of the initial Hg^{2+} calculated from the pseudo-second-order model were 21.3, 20.6, 26.8, 30.8, and 38.7 mg/g for CG, RHB, RHB/CG-10:1, RHB/CG-5:1, and RHB/CG-1:1, respectively, which were slightly higher than those estimated by the pseudo-first-order model and more consistent with the experimental adsorption behavior. These results imply that chemisorption may play a dominant role in the Hg^{2+} adsorption process. For chemisorption-dominated materials, solution pH is a critical factor affecting Hg^{2+} removal (Figure 5b). Combined with the PHREEQC simulation results (Figure 6a,b, 1 mg/L total Hg, 0.355 mg/L Cl^-), in the weakly acidic to neutral range (pH 4–10), the neutral $Hg(OH)_2$ and HgClOH species predominates. Being uncharged, it avoids competition with H^+, while the deprotonated surface functional groups (e.g., -OH, -COOH) on biochar exhibit the strongest electrostatic attraction and coordination toward Hg^{2+}, leading to maximum adsorption capacity and removal efficiency. At very low pH (<3), $HgCl^+$ and $HgCl_2$ are the main species. However, abundant H^+ ions compete for active sites and protonate functional groups, severely inhibiting chemisorption—resulting in decreased removal. At high pH (>8), Hg^{2+}

tends to form hydroxide precipitates ($Hg(OH)_2$), and while total mercury removal may appear high due to precipitation, the genuine contribution of chemisorption decreases, and the negatively charged $Hg(OH)_3^-$ species experiences electrostatic repulsion from the deprotonated surface.

Table 2. Fitting parameters of the pseudo-first-order and pseudo-second-order kinetic models for pollutant adsorption onto RHB and RHB/CG composite biochars, including the correlation coefficient (R^2) and equilibrium adsorption capacity (mg/g) at 1 mg/L of initial Hg^{2+} concentration.

Adsorbent	Pseudo-First-Order Kinetic Model		Pseudo-Second-Order Kinetic Model	
	R^2	Equilibrium Adsorption Capacity at 1 mg/L	R^2	Equilibrium Adsorption Capacity at 1 mg/L
CG	0.995	18.6	0.995	21.3
RHB	0.975	19.7	0.991	20.6
RHB/CG-10:1	0.991	25.7	0.997	26.8
RHB/CG-5:1	0.986	30.4	0.994	30.8
RHB/CG-1:1	0.986	36.7	0.997	38.7

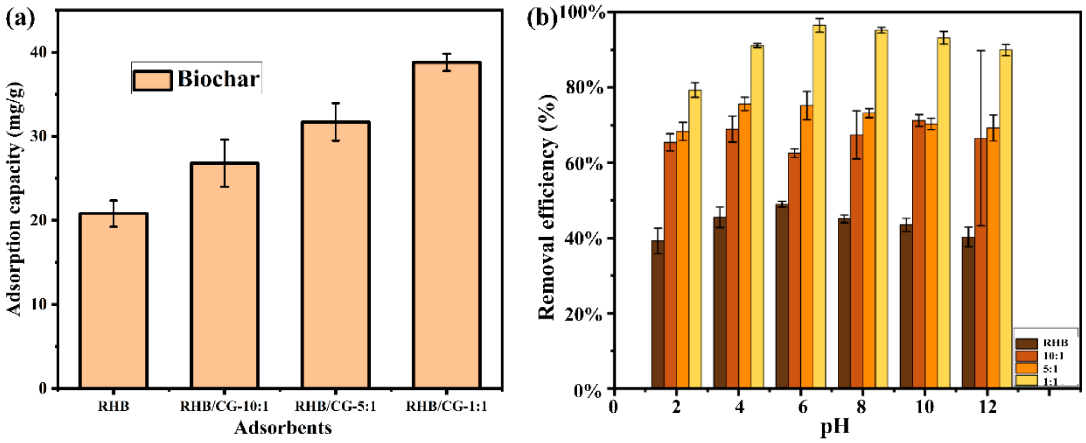


Figure 5. (**a**) Comparison of Hg^{2+} adsorption capacities of RHB and RHB/CG composite biochars. (**b**) Effect of solution pH on Hg^{2+} removal by RHB, RHB/CG-10:1, RHB/CG-5:1, and RHB/CG-1:1.

The incorporation of coal gangue significantly enhanced the Hg^{2+} adsorption capacity of the biochar composites. The adsorption capacities followed the order of RHB < RHB/CG-10:1 < RHB/CG-5:1 < RHB/CG-1:1, indicating that higher coal gangue addition resulted in better adsorption performance (Figure 5a). Meanwhile, under the same experimental conditions, the equilibrium adsorption capacity at 1 mg/g of initial Hg^{2+} for raw coal gangue was only 21.3 mg/g, demonstrating its limited adsorption capacity (Table 2). Specifically, the maximum adsorption capacity increased from 20.6 mg/g for pristine RHB to 38.7 mg/g for RHB/CG-1:1 based on the pseudo-second-order model. This improvement is likely related to the formation of additional metal oxide-related phases and Si–O–M structures during co-pyrolysis, which not only provide more chemisorption sites but may also alter the pH response of the material. Compared with pristine RHB, RHB/CG composites are expected to have a broader effective pH range from 4 to 12 and can partially alleviate H^+ competition under acidic conditions due to the presence of local alkaline sites or Lewis acid sites. Therefore, in practical Hg^{2+}-contaminated water treatment, RHB/CG composites are expected to exhibit better adaptability and stability over a wider pH range.

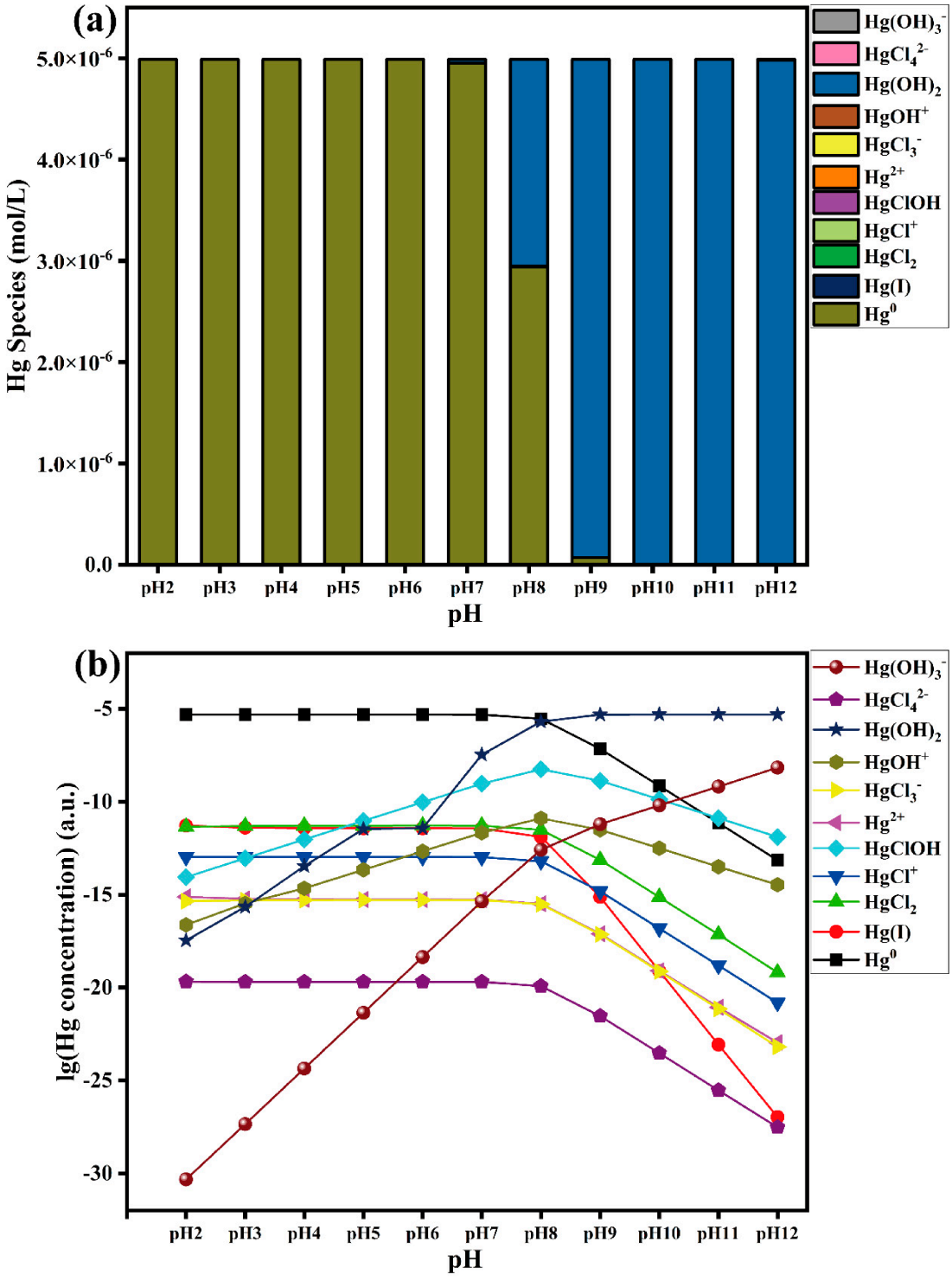


Figure 6. The pH-dependent speciation of mercury was simulated using PHREEQC for an aqueous system containing 1 mg/L total Hg and 0.355 mg/L Cl^-. (**a**) Distribution of dissolved Hg species as concentrations (mol/L) across pH 2–12. (**b**) Log-transformed concentrations of individual Hg species as a function of pH. The results indicate a clear transition in dominant Hg species with increasing pH, from reduced elemental mercury and chloride/hydroxyl complexes under acidic to near-neutral conditions to hydroxylated species, particularly $Hg(OH)_2$, under alkaline conditions.

3.4. Coal Gangue Suppressing Hg^{2+} Reduction

The distribution of mercury species in a $HgCl_2$ solution as a function of pH was simulated using PHREEQC 3.7 under an assumed pe of 6.0, a moderately oxidizing condition, not representing the actual unknown redox state of the reaction solution. The simulation

results indicate that under this hypothetical condition, some reductants would thermodynamically favor the reduction of Hg^{2+} to Hg^0 in the neutral to acidic pH range (Figure 6a,b). However, in the control experiments without biochar, the actual generation of Hg^0 was negligible, suggesting that the thermodynamically predicted speciation is only realized in the presence of electron donors. Upon the introduction of biochar, both pristine RHB and the RHB/CG composite produced measurable amounts of Hg^0 (ranging from 0.12 to 0.28 mg/L) (Figure 7a,b), confirming that biochar surfaces can act as electron donors to drive the reduction of Hg^{2+}.

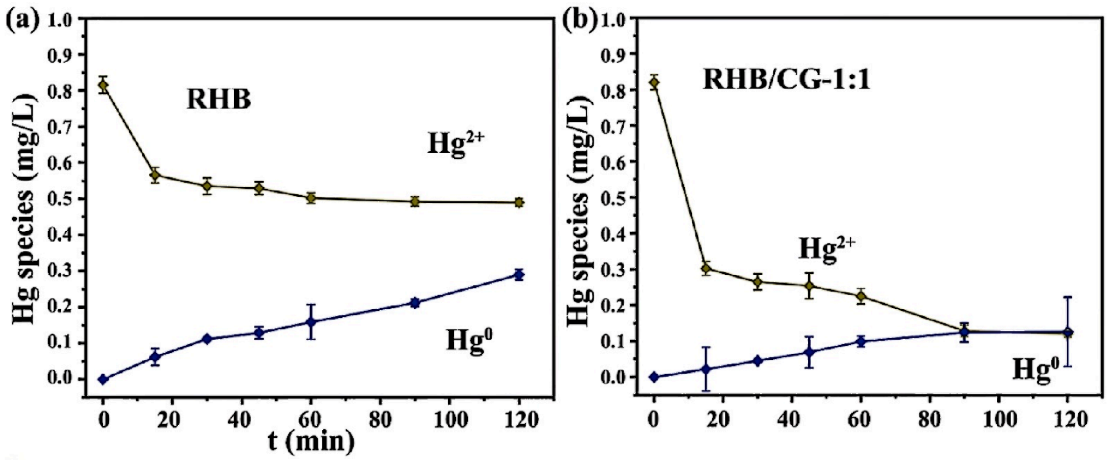


Figure 7. Time-dependent concentration changes of mercury species (Hg^{2+} and Hg^0) in the presence of (**a**) RHB and (**b**) RHB/CG-1:1.

Notably, the pristine RHB system accumulated significantly more Hg^0 than the RHB/CG system, whereas RHB/CG exhibited a faster removal rate of Hg^{2+}. This contrast indicates that although the reduction reaction is thermodynamically favorable, the surface chemical properties of the material can effectively modulate the kinetic pathway and extent of the reaction. The RHB/CG composite is rich in basic functional groups, including C–O–C and Si–O–M mineral structures, which may inhibit Hg^{2+} reduction through the following mechanisms: (i) preferentially sequestering Hg^{2+} via coordination, reducing its residence time on reduction sites, and (ii) interfering with the electron transfer pathways from the biochar surface to Hg^{2+}. Notably, during co-pyrolysis, the metal elements (e.g., Fe, Al) from coal gangue are incorporated into the carbon matrix via stable M–O–C covalent bonds rather than existing as discrete, surface-exposed oxide particles. This structural integration passivates the otherwise electron-donating capacity of the biochar matrix and limits any independent redox activity of mineral phases. Consequently, RHB/CG not only shows faster adsorption kinetics and higher adsorption capacity but also effectively suppresses the formation of volatile Hg^0, which is of great significance for controlling the dispersion of Hg in practical environmental remediation.

4. Conclusions and Perspectives

In this study, coal gangue and rice husk were co-pyrolyzed to prepare composite biochars (RHB/CG) for aqueous Hg^{2+} removal. FTIR and XRD results revealed that coal gangue incorporation promoted the evolution of oxygen-containing functional groups (C–O, $–COO^-$) and generated metal oxide phases such as Fe–O, Al–O, and Si–O–M on the biochar surface, while Raman spectra indicated that the carbon skeleton remained largely intact. Adsorption kinetics followed the pseudo-second-order model (R^2 = 0.991–0.997), confirming chemisorption as the dominant mechanism. The equilibrium adsorption capacity of RHB/CG-1:1 (38.7 mg/g) was substantially higher than that of pristine RHB (20.6 mg/g),

and the capacity increased with the increasing coal gangue ratio. pH-dependent experiments combined with PHREEQC simulations (pe = 6.0, pH 2–12) demonstrated that optimal adsorption occurred in the weakly acidic to neutral range (pH 4–7) where neutral $Hg(OH)_2$ prevails, and the composite exhibited better adaptability over a broader pH range.

More importantly, RHB/CG composites effectively suppressed the reduction of Hg^{2+} to volatile Hg^0. In time-dependent kinetic experiments, the Hg^0 concentration in the RHB/CG system (<0.12 mg/L) was significantly lower than that in the pristine RHB system (up to 0.28 mg/L), while the Hg^{2+} removal rate was faster. Mechanistically, the basic functional groups (C–O–C, Si–O–M) on RHB/CG inhibited reduction by raising the local pH, preferentially sequestering Hg^{2+} via coordination, and interfering with electron transfer pathways from reductive sites (e.g., quinone–hydroquinone moieties) in biochar. Consequently, RHB/CG offers the dual advantages of high adsorption efficiency and suppressed mercury volatilization, reducing the risk of secondary Hg^0 release and dispersion. It represents a low-cost, easy-to-prepare, and environmentally friendly material option for treating mercury-contaminated wastewater and remediating polluted sites.

However, several limitations of this study should be acknowledged. Adsorption isotherms were not conducted, so the true maximum adsorption capacity remains unknown. The reported values are equilibrium uptakes at a single initial concentration. No validation experiments using real-water matrices (e.g., river water, groundwater, or industrial wastewater) were performed, and thus the influence of coexisting ions and natural organic matter on performance has not been assessed. The kinetic data lack high-resolution sampling during the initial 0–10 min period, which prevented reliable quantitative intraparticle diffusion (IPD) analysis. Additionally, BET surface area and XRF bulk composition analyses were not carried out, limiting a complete structure–property correlation. Long-term stability, reusability, and cost analysis were also not evaluated. Future work will address these gaps through isotherm experiments, real-water validation, higher-resolution kinetics, and additional characterization.

Author Contributions: Conceptualization, K.Z., W.Y. and S.H.; methodology, Y.Z., P.H. and F.X.; validation, S.S.; formal analysis, P.H.; investigation, W.Y., J.Y., Y.Z. and J.Z.; data curation, J.Y.; writing—review and editing, S.S., Y.H. and S.H.; visualization, K.Z., F.X., Y.H. and J.Z.; supervision, K.Z. and S.S.; project administration, K.Z.; funding acquisition, K.Z. All authors have read and agreed to the published version of the manuscript.

Funding: This work was supported by the National Natural Science Foundation of China Youth Fund Category C (Grant No. 42207247) and the Fundamental Research Funds for the Central Universities (Grant No. 2025QN1113).

Data Availability Statement: The original contributions presented in this study are included in the article. Further inquiries can be directed to the corresponding authors.

Conflicts of Interest: Author Shunquan Shi was employed by the China Water Resources Pearl River Planning Surveying and Designing Co., Ltd. The remaining authors declare that we have no financial and personal relationships with other people or organizations that can inappropriately influence our work, and there is no professional or other personal interest of any nature or kind in any product, service and/or company that could be construed as influencing the position presented in, or the review of, the manuscript entitled "Surface Chemical Regulation of Coal Gangue–Rice Husk Biochar for Concurrent Promotion of Hg^{2+} Adsorption and Inhibition of Hg^0 Production".

References

1. Liu, N.; Li, X.; Chen, P.; Yuan, W.; Lin, C.J.; Feng, X.; Wang, X. Mercury Transport, Transformation and Accumulation Recorded by Stable Isotopes during Retreated Glacier Chronosequence of 250 Years. *Environ. Sci. Technol.* **2025**, *59*, 6085–6096. [CrossRef] [PubMed]

2. Chen, L.; Zhou, J.; Guo, L.; Bian, X.; Xu, Z.; Chen, Q.; Wen, S.H.; Wang, K.; Liu, Y.R. Global Distribution of Mercury in Foliage Predicted by Machine Learning. *Environ. Sci. Technol.* **2024**, *58*, 15629–15637. [CrossRef] [PubMed]
3. Jetashree; Zhong, Q.; Zhou, H.; Li, Y.; Liu, Y.; Li, J.; Liang, S. Role of Trade in India's Rising Atmospheric Mercury Emissions. *Environ. Sci. Technol.* **2022**, *56*, 790–803. [CrossRef] [PubMed]
4. Sun, R.; Cao, F.; Dai, S.; Shan, B.; Qi, C.; Xu, Z.; Li, P.; Liu, Y.; Zheng, W.; Chen, J. Atmospheric Mercury Isotope Shifts in Response to Mercury Emissions from Underground Coal Fires. *Environ. Sci. Technol.* **2023**, *57*, 8638–8649. [CrossRef] [PubMed]
5. Shen, J.; Yin, R.; Algeo, T.J.; Svensen, H.H.; Schoepfer, S.D. Mercury evidence for combustion of organic-rich sediments during the end-Triassic crisis. *Nat. Commun.* **2022**, *13*, 1307. [CrossRef] [PubMed]
6. Dal Corso, J.; Mills, B.J.W.; Chu, D.; Newton, R.J.; Mather, T.A.; Shu, W.; Wu, Y.; Tong, J.; Wignall, P.B. Permo-Triassic boundary carbon and mercury cycling linked to terrestrial ecosystem collapse. *Nat. Commun.* **2020**, *11*, 2962. [CrossRef] [PubMed]
7. Meyer, K.W.; Petersen, S.V.; Lohmann, K.C.; Blum, J.D.; Washburn, S.J.; Johnson, M.W.; Gleason, J.D.; Kurz, A.Y.; Winkelstern, I.Z. Biogenic carbonate mercury and marine temperature records reveal global influence of Late Cretaceous Deccan Traps. *Nat. Commun.* **2019**, *10*, 5356. [CrossRef] [PubMed]
8. Szponar, N.; Vega, C.M.; Gerson, J.; McLagan, D.S.; Pillaca, M.; Delgado, S.; Lee, D.; Rahman, N.; Fernandez, L.E.; Bernhardt, E.S.; et al. Tracing Atmospheric Mercury from Artisanal and Small-Scale Gold Mining. *Environ. Sci. Technol.* **2025**, *59*, 5021–5033. [CrossRef] [PubMed]
9. Ouyang, D.; Wu, Q.; Wang, S.; Cui, Y.; Liu, K.; Wu, W.; Li, S.; Shi, Z.; Wen, M. Multimedia Mercury Emissions from Key Industries in China and Implications for Mercury Control. *Environ. Sci. Technol.* **2025**, *59*, 22544–22553. [CrossRef] [PubMed]
10. Sahu, S.K.; Mishra, M.; Mishra, A.; Mangaraj, P.; Beig, G. Quantification and assessment of hazardous mercury emission from industrial process and other unattended sectors in India: A step towards mitigation. *J. Hazard. Mater.* **2024**, *470*, 134103. [CrossRef] [PubMed]
11. Outridge, P.M.; Mason, R.P.; Wang, F.; Guerrero, S.; Heimburger-Boavida, L.E. Updated Global and Oceanic Mercury Budgets for the United Nations Global Mercury Assessment 2018. *Environ. Sci. Technol.* **2018**, *52*, 11466–11477. [CrossRef] [PubMed]
12. Schneider, L.; Guerrero, S.; Mudd, G.; Lopez, M.A.A.; Beck, K.K.; Sun, R.; Haberle, S.G.; Fletcher, M.S.; Zawadzki, A.; Hintelmann, H.; et al. The Legacy of Mercury Contamination from Colonial Nonferrous Mining in the Southern Hemisphere. *Environ. Sci. Technol.* **2025**, *59*, 13275–13285. [CrossRef] [PubMed]
13. García, O.; Veiga, M.M.; Cordy, P.; Suescún, O.E.; Molina, J.M.; Roeser, M. Artisanal gold mining in Antioquia, Colombia: A successful case of mercury reduction. *J. Clean. Prod.* **2015**, *90*, 244–252. [CrossRef]
14. Diringer, S.E.; Berky, A.J.; Marani, M.; Ortiz, E.J.; Karatum, O.; Plata, D.L.; Pan, W.K.; Hsu-Kim, H. Deforestation Due to Artisanal and Small-Scale Gold Mining Exacerbates Soil and Mercury Mobilization in Madre de Dios, Peru. *Environ. Sci. Technol.* **2020**, *54*, 286–296. [CrossRef] [PubMed]
15. Javier, G.-B.; Juan, V.-V.; Margareth, D.-I.; Lucellys, S.-M.; Jesus, O.-V. Environmental Pollution by Mercury and Trace Metals in Highly Vulnerable Afro-Descendant Territories in the Department of Cauca, Colombia. *Soil Sediment Contam. Int. J.* **2024**, *34*, 510–527. [CrossRef]
16. Hammer, V.; Vanneste, J.; Alejo-Zapata, F.D.; Zea, J.; Bolaños-Sosa, H.G.; Zevallos Rojas, C.A.; Figueroa, L.A.; Malone, A.; Bellona, C.; Vuono, D.C. Characterization of medium and small-scale gold processing operations, wastewaters, and tailings in the Arequipa region of Peru. *Sci. Total Environ.* **2024**, *945*, 174034. [CrossRef] [PubMed]
17. Manohar, D.M.; Anoop Krishnan, K.; Anirudhan, T.S. Removal of mercury(II) from aqueous solutions and chlor-alkali industry wastewater using 2-mercaptobenzimidazole-clay. *Water Res.* **2002**, *36*, 1609–1619. [CrossRef] [PubMed]
18. Fan, W.; Kou, M.; Wang, Y.; Liu, Y.; Zhang, Q.; Guo, Y.; Yin, Y.; Cai, Y.; Jiang, G. Microbial methylation of particulate-bound mercury in water column and its underlying mechanisms: A critical review. *Water Res.* **2026**, *289*, 124871. [CrossRef] [PubMed]
19. Lavergne, C.; Rodriguez-Puig, J.; Ruiz-Gonzalez, C.; Montero-Curiel, M.; Casas, G.; Romano-Gude, D.; Alorda-Montiel, I.; Dordal-Soriano, J.; Alorda-Kleinglass, A.; Diego-Feliu, M.; et al. Unveiling Hidden Mercury and Methylmercury Sources: The Role of Submarine Groundwater Discharge in Coastal Lagoons. *Environ. Sci. Technol.* **2025**, *59*, 20653–20664. [CrossRef] [PubMed]
20. Wang, J.; Xie, Q.; Xiang, Y.; Xue, J.; Jiang, T.; Zhang, C.; Li, J.; Wang, Y.; Wang, D. Anthropogenic activities enhance mercury methylation in sediments of a multifunctional lake: Evidence from dissolved organic matter and mercury-methylating microorganisms. *J. Hazard. Mater.* **2024**, *466*, 133505. [CrossRef] [PubMed]
21. Willacker, J.J.; Eagles-Smith, C.A.; Baldwin, A.K.; Tate, M.T.; Poulin, B.A.; Naymik, J.; Krabbenhoft, D.P.; Myers, R.; Chandler, J.A. Contrasting Magnitude and Timing of Pulsed Aqueous Methylmercury Bioaccumulation across a Reservoir Food Web. *Environ. Sci. Technol.* **2025**, *59*, 3884–3894. [CrossRef] [PubMed]
22. Zhang, T.; Kim, B.; Levard, C.; Reinsch, B.C.; Lowry, G.V.; Deshusses, M.A.; Hsu-Kim, H. Methylation of mercury by bacteria exposed to dissolved, nanoparticulate, and microparticulate mercuric sulfides. *Environ. Sci. Technol.* **2012**, *46*, 6950–6958. [CrossRef] [PubMed]
23. Liu, L.; Chen, G.; Hu, H.; Huang, Y. Investigation of elemental mercury removal performance and mechanism of rice straw biochars from a fluidized bed pyrolysis system impregnated by NH4Br. *Chem. Eng. J.* **2024**, *492*, 152069. [CrossRef]

24. Niu, Q.; Yang, T.; Chen, D.D.; Zhu, X.J.; Guo, Y.; Chen, X.E.; Xu, B.; Liu, C.G. Utilizing non-thermal plasma to introduce chlorine-containing functional groups on multi-walled carbon nanotubes for enhanced elemental mercury removal. *Sustain. Chem. Pharm.* **2024**, *41*, 101695. [CrossRef]
25. Yang, N.N.; Shin, C.H.; Kim, D.; Park, J.S.; Rao, P.H.; Wang, R.K. Synthesis, characterization, and mercury removal application of surface modified kapok fibers with dopamine (DA): Investigation of bidentate adsorption. *Environ. Earth Sci.* **2020**, *79*, 264. [CrossRef]
26. Huang, Y.; Zhao, B.; Liu, G.; Liu, K.; Dang, B.; Lyu, H.; Tang, J. Effective reducing the mobility and health risk of mercury in soil under thiol-modified biochar amendment. *J. Hazard. Mater.* **2024**, *462*, 132712. [CrossRef] [PubMed]
27. Samad, K.A.; Salleh, I.S.M.; Zahari, M.; Yussof, H.W. Batch study on the removal of mercury (II) ion from industrial wastewater using activated palm oil fuel ash. *Mater. Today Proc.* **2019**, *17*, 1126–1132. [CrossRef]
28. Yaghmaeian, K.; Mashizi, R.K.; Nasseri, S.; Mahvi, A.H.; Alimohammadi, M.; Nazmara, S. Removal of inorganic mercury from aquatic environments by multi-walled carbon nanotubes. *J. Environ. Health Sci. Eng.* **2015**, *13*, 55. [CrossRef] [PubMed]
29. Chen, X.; Alvarez, P.J.J.; Masiello, C.A. Environmentally Persistent Free Radicals in Biochar: Environmental Context and Future Research Needs. *Environ. Sci. Technol.* **2025**, *59*, 11440–11454. [CrossRef] [PubMed]
30. Chen, H.; Xu, J.; Yuan, J.; Wang, L.; Chen, G.; Turner, B.L.; Wang, S.; Wang, Y. Long-Term Biochar Application Enhances Carbon-Phosphorus Costabilization and Mitigates Methane Emissions in Flooded Rice Systems. *Environ. Sci. Technol.* **2026**, *60*, 7872–7883. [CrossRef] [PubMed]
31. Cheng, Y.; Deng, B.; Scotland, P.; Eddy, L.; Hassan, A.; Wang, B.; Silva, K.J.; Li, B.; Wyss, K.M.; Ucak-Astarlioglu, M.G.; et al. Electrothermal mineralization of per- and polyfluoroalkyl substances for soil remediation. *Nat. Commun.* **2024**, *15*, 6117. [CrossRef] [PubMed]
32. Magee, J.C.; Seenthia, N.I.; Wadzuk, B.; Hamidi, D.; He, K.; Blaney, L.; Xu, W. Tailored carbonaceous materials as biofilter amendments for PFAS removal in stormwater runoff. *Water Res.* **2026**, *288*, 124569. [CrossRef] [PubMed]
33. Luo, Z.; Yao, B.; Yang, X.; Wang, L.; Xu, Z.; Yan, X.; Tian, L.; Zhou, H.; Zhou, Y. Novel insights into the adsorption of organic contaminants by biochar: A review. *Chemosphere* **2022**, *287*, 132113. [CrossRef] [PubMed]
34. Wang, Y.; Joseph, S.; Wang, X.; Weng, Z.H.; Mitchell, D.R.G.; Nancarrow, M.; Taherymoosavi, S.; Munroe, P.; Li, G.; Lin, Q.; et al. Inducing Inorganic Carbon Accrual in Subsoil through Biochar Application on Calcareous Topsoil. *Environ. Sci. Technol.* **2023**, *57*, 1837–1847. [CrossRef] [PubMed]
35. Luo, L.; Wang, J.; Lv, J.; Liu, Z.; Sun, T.; Yang, Y.; Zhu, Y.-G. Carbon Sequestration Strategies in Soil Using Biochar: Advances, Challenges, and Opportunities. *Environ. Sci. Technol.* **2023**, *57*, 11357–11372. [CrossRef] [PubMed]
36. O'Connor, D.; Peng, T.; Li, G.; Wang, S.; Duan, L.; Mulder, J.; Cornelissen, G.; Cheng, Z.; Yang, S.; Hou, D. Sulfur-modified rice husk biochar: A green method for the remediation of mercury contaminated soil. *Sci. Total Environ.* **2018**, *621*, 819–826. [CrossRef] [PubMed]
37. Li, L.; Wang, X.; Fu, H.; Qu, X.; Chen, J.; Tao, S.; Zhu, D. Dissolved Black Carbon Facilitates Photoreduction of Hg(II) to Hg(0) and Reduces Mercury Uptake by Lettuce (*Lactuca sativa* L.). *Environ. Sci. Technol.* **2020**, *54*, 11137–11145. [CrossRef] [PubMed]
38. Zhang, K.; Wang, L.; Qin, M.; Mulder, J.; Hou, D. Mercury reduction by black carbon under dark conditions. *Water Res.* **2023**, *242*, 120241. [CrossRef] [PubMed]
39. Zhang, Z.; Li, J.; Zhang, X. Rapid removal of low concentration Hg(II) from water by iron nanoparticles: Excellent performance and unique mechanism. *Chem. Eng. J.* **2023**, *471*, 144643. [CrossRef]
40. Yu, J.; Wu, Z.; An, X.; Tian, F.; Yu, B. Trace metal elements mediated co-pyrolysis of biomass and bentonite for the synthesis of biochar with high stability. *Sci. Total Environ.* **2021**, *774*, 145611. [CrossRef] [PubMed]
41. Zhang, X.; Lei, H.; Chen, S.; Wu, J. Catalytic co-pyrolysis of lignocellulosic biomass with polymers: A critical review. *Green Chem.* **2016**, *18*, 4145–4169. [CrossRef]
42. Chen, M.; Zhou, Y.; Sun, Y.; Chen, X.; Yuan, L. Coal gangue-based magnetic porous material for simultaneous remediation of arsenic and cadmium in contaminated soils: Performance and mechanisms. *Chemosphere* **2023**, *338*, 139380. [CrossRef] [PubMed]
43. Jablonska, B.; Kityk, A.V.; Busch, M.; Huber, P. The structural and surface properties of natural and modified coal gangue. *J. Environ. Manag.* **2017**, *190*, 80–90. [CrossRef] [PubMed]
44. Herrera, K.; Morales, L.F.; Tarazona, N.A.; Aguado, R.; Saldarriaga, J.F. Use of Biochar from Rice Husk Pyrolysis: Part A: Recovery as an Adsorbent in the Removal of Emerging Compounds. *ACS Omega* **2022**, *7*, 7625–7637. [CrossRef] [PubMed]
45. Zhang, K.; Sun, P.; Khan, A.; Zhang, Y. Photochemistry of biochar during ageing process: Reactive oxygen species generation and benzoic acid degradation. *Sci. Total Environ.* **2021**, *765*, 144630. [CrossRef] [PubMed]
46. Wang, L.; Yang, J.; Li, X.; Zhang, L.; Van Zwieten, L.; Mašek, O.; Joseph, S.; Zhang, K.; Yu, K. Engineered biochar composite with minerals: Organo-mineral interactions, physicochemical changes, and implications for practical application. *Biochar* **2026**, *8*, 53. [CrossRef]

47. Zhang, Y.; Yang, W.; Zhang, K.; Kumaravel, A.; Zhang, Y. Sulfite Activation by Glucose-Derived Carbon Catalysts for As(III) Oxidation: The Role of Ketonic Functional Groups and Conductivity. *Environ. Sci. Technol.* **2021**, *55*, 11961–11969. [CrossRef] [PubMed]
48. Zhang, K.; Sun, P.; Faye, M.C.A.S.; Zhang, Y. Characterization of biochar derived from rice husks and its potential in chlorobenzene degradation. *Carbon* **2018**, *130*, 730–740. [CrossRef]
49. Zhang, K.; Khan, A.; Sun, P.; Zhang, Y.; Taraqqi, A.K.A.; Zhang, Y. Simultaneous reduction of Cr(VI) and oxidization of organic pollutants by rice husk derived biochar and the interactive influences of coexisting Cr(VI). *Sci. Total Environ.* **2020**, *706*, 135763. [CrossRef] [PubMed]
50. Zhang, K.; Sun, P.; Zhang, Y.; Murugananthan, M.; Ammasai, K.; Zhang, Y. Enhancement of S(IV)-Cr(VI) reaction in p-nitrophenol degradation using rice husk biochar at neutral conditions. *Sci. Total Environ.* **2020**, *749*, 142086. [CrossRef] [PubMed]
51. Villars, P.; Cenzual, K.; Daams, J.; Gladyshevskii, R.; Savysyuk, I. Ca2Fe22O33. In *Landolt-Börnstein-Group III Condensed Matter*; Springer: Berlin/Heidelberg, Germany, 2010; p. 393.
52. Profeta, D.O.; da Silva, M.A.; Faria, D.N.; Cipriano, D.F.; Freitas, J.C.C.; dos Santos, F.S.; Lima, T.M.; Vasconcelos, S.C.; Pietre, M.K. Zeolite/calcium carbonate composite for a synergistic adsorption of cadmium in aqueous solution. *Next Mater.* **2025**, *6*, 100493. [CrossRef]

Disclaimer/Publisher's Note: The statements, opinions and data contained in all publications are solely those of the individual author(s) and contributor(s) and not of MDPI and/or the editor(s). MDPI and/or the editor(s) disclaim responsibility for any injury to people or property resulting from any ideas, methods, instructions or products referred to in the content.